

Graphene Modified Montmorillonite Based Phase Change Material for Thermal Energy Storage with Enhanced Interfacial Thermal Transfer

Kang Peng

Xi'an Jiaotong University

Hongjie Wang (✉ hjwang@mail.xjtu.edu.cn)

Xi'an Jiaotong University

Pengfei wan

Xi'an Jiaotong University

Jianwei Wang

Xi'an Jiaotong University

Hua Luo

Xi'an Jiaotong University

Senhai Zhou

Xi'an Jiaotong University

Xiaoyu Li

Chang'an University

Jun Yang

Xi'an University of Architecture and Technology

Nano Express

Keywords: Montmorillonite, Graphene, Phase change material, Thermal energy storage, Interfacial thermal transfer

Posted Date: February 6th, 2020

DOI: <https://doi.org/10.21203/rs.2.22797/v1>

License: © ⓘ This work is licensed under a Creative Commons Attribution 4.0 International License.

[Read Full License](#)

Abstract

Thermal energy storage technology plays a crucial role in the thermal management system. Clay based organic phase change material has considerable advantages in the application of thermal energy storage due to low cost and high energy storage capacity. However, the low thermal conductivity of clay, especially poor interfacial thermal transfer, limits its thermal energy storage efficiency. Herein, stearic acid/reduced graphene oxide modified montmorillonite composites (SA/RGO-MMT) were prepared by the vacuum impregnation of stearic acid into graphene modified montmorillonite matrix, which was obtained via the in situ reduction of graphene oxide on the surface of montmorillonite. Stearic acid is assembled in the porous structures of RGO-MMT with the physical interactions. SA/RGO-MMT possesses high melting enthalpy of 159 J/g, low extent of supercooling of 1.4 °C and excellent thermal reliability after 100 thermal cycling. Energy storage and release rates of SA/RGO-MMT were significantly improved due to the enhanced interfacial thermal transfer by graphene. Therefore, SA/RGO-MMT is a promising form-stable phase change material for applications in solar heat storage fields. The strategy in this study highlights the importance of enhancing interfacial thermal transfer for the efficient thermal energy storage materials.

Background

In the past decade, thermal management has become emerging subject and attracted tremendous attention from fundamental research and industrial applications[1]. As part of thermal management systems, thermal energy storage technology has received significant interest due to its crucial role in the solar thermal technology and building energy conservation[2]. Phase change material (PCM) could store and release thermal energy through a phase change process (such as melting and solidification) at a relatively stable temperature, which makes it a kind of promising thermal energy storage material[3, 4].

Among a variety of PCM, organic phase change materials, such as fatty acid, paraffin wax, alkane and polyethylene glycol demonstrate great advantages due to nontoxicity[5], reusability[6], high thermal storage capacity[7], small temperature and volume change during energy storage and release processes[8]. However, the efficient energy storage and release applications of organic phase change materials are restricted by their poor mechanical stability and low thermal conductivity, which could lead to potential leakage risk and low energy storage rate during phase change process. An effective solution is constructing form-stable phase change material via loading organics into various supporting materials[9], such as graphene[10], carbon nanotube[11], mesoporous silica[12, 13] and porous minerals[14].

As one of abundant clay mineral, montmorillonite (MMT) possesses natural 2D lamellar morphology, of which structural unit layers consist two SiO_4 tetrahedral sheets and a central $\text{AlO}_4(\text{OH})_2$ octahedral sheet[15–17]. It is a promising supporting material for loading organic phase change materials due to its plentiful porous structure[18], high surface area[19], appropriate surface property[20] and lower cost[21–24]. Yi Wang et al[25] prepared two kinds of activated montmorillonite based phase change materials via

melting impregnation method, which contain 47.5wt.% and 46.9 wt.% stearic acid and has relatively reliable thermal stability. However, the low thermal conductivity of MMT, especially poor interfacial thermal transfer, limits the thermal energy storage rate of montmorillonite based phase change materials.

Graphite, as a natural non-metallic mineral, has relatively high thermal conductivity, which could be utilized as supporting material for phase change material independently and cooperatively[26]. Su-Gwang Jeong et al[27] used sodium montmorillonite and exfoliated graphite as the supporting material to prepare shaped stabilized phase change material via a vacuum impregnation method, which could improve the thermal conductivity and prevent leakage of phase change material. However, graphite might not be distributed uniformly by mixing simply montmorillonite and graphite with organics, and the interfacial thermal transfer between montmorillonite and organics could be bottleneck for a heat transfer. Graphene with extremely high thermal conductivity ($5150 \text{ W m}^{-1} \text{ K}^{-1}$)[28, 29] might be an ideal material to enhance thermal transfer efficiency of montmorillonite based phase change materials[30, 31]. Therefore, surface of montmorillonite could be modified by graphene, which might enhance interfacial thermal transfer between montmorillonite and organics.

In this study, we prepared reduced graphene oxide modified montmorillonite (RGO-MMT) by the in situ reduction of graphene oxide on the surface of MMT, which was used to load organic phase change materials via vacuum impregnation method. The microstructure and morphology obtained stearic acid/reduced graphene oxide modified montmorillonite composites (SA/RGO-MMT) were characterized, and the performances of thermal energy storage and release were evaluated. The role of graphene for enhancing the interfacial thermal transfer between montmorillonite and organics was investigated, and the possible mechanism of thermal transfer in the composite phase-change material was explored.

Methods

Materials

Na-montmorillonite used was provided by Zhejiang Sanding Technology Co. Ltd. (Zhejiang, China). Graphene oxide (GO) was prepared by the modified Hummers' method[32]. Sodium borohydride (NaBH_4) and stearic acid (SA, $\text{C}_{18}\text{H}_{36}\text{O}_2$) were purchased from Sinopharm Chemical Reagent Co. Ltd. All reagents were used without further purification.

Preparation

Stearic acid/reduced graphene oxide modified montmorillonite composites (SA/RGO-MMT) were prepared by loading SA into RGO-MMT matrix, which was obtained via the in situ reduction of GO on the surface of MMT. In a typical experiment, 1.000 g of MMT was dispersed in to 100 mL of GO solution (about 1 mg/mL), and the mixed suspension was stirred for 24 h at 30 °C. Then, 2.000 g of NaBH_4 was added into the suspension under magnetic stirring for 7 h at 95 °C. The suspension was filtered and dried at 60 °C for 24 h to obtain the RGO-MMT. SA was loaded into RGO-MMT by the vacuum impregnation method. 5.000 g of SA and 1.000 g of RGO-MMT were mixed and added into a conical flask (100 mL in

capacity), and the conical flask was maintained at 90 °C for 1 h with the air pressure of -0.1 MPa. The mixtures were thermally filtered at 90 °C for 24 h to remove the leaked SA, and the SA/RGO-MMT form-stable phase change material was obtained finally. For comparison, SA/MMT composites were prepared by a similar method.

Characterization

The morphologies of the samples were observed by scanning electron microscope (SEM, JEOL JSM-6360LV) under the accelerating voltage of 5 kV and transmission electron microscope (TEM, JEOL JEM-2100F) at 200 kV. The powder X-ray diffraction (XRD) measurements of the samples were operated with a RIGAKU D/max-2550 PC X-ray diffractometer, using Cu K α radiation ($\lambda = 0.15406$ nm). Fourier transform infrared (FTIR) spectra were recorded by a Nicolet Nexus 670 FTIR spectrophotometer with KBr pellets. Differential scanning calorimetry (DSC) was performed on a NETZSCH DSC 200 F3 Maia instrument with the heating rate of 1 °C/min in the atmosphere of argon.

Evaluation of the energy storage performance

The heat storage and release performances were evaluated via measuring the temperature variation during the phase change process. In the test, the sample was putted into a test tube at the ambient temperature. Then, the test tube was maintained at 80 °C. The temperature of sample was monitored by as temperature recorder (SSN-11E). After the temperature of sample was raised to about 80 °C, the test tube was taken out and cooled naturally to the ambient temperature. The heat storage stability of sample was evaluated via comparison the properties of sample before and after 100 thermal cycling. The thermal cycling test was carried out in a test tube, which was heated to 80 °C and cooled to the ambient temperature repeatedly.

Results And Discussion

As illustrated in Fig. 1, graphene oxide in the aqueous phase was adsorbed on the surface of MMT via the hydrogen bond due to the surface hydroxyl group. After the graphene oxide was in situ reduced by NaBH₄, the surface of MMT was modified with reduced graphene oxide. Reduced graphene oxide modified montmorillonite (RGO-MMT) was used as supporting material to load stearic acid (SA) via vacuum impregnation method. Reduced graphene oxide connects between SA and MMT as thermal transfer bridge at the interface of obtained SA/RGO-MMT form-stable phase change material. For comparison, stearic acid/montmorillonite (SA/MMT) was prepared via similar vacuum impregnation method without graphene.

The morphologies of samples were observed by scanning electron microscope (SEM) and transmission electron microscopy (TEM). As shown in the SEM and TEM images (Fig. 2a and b), MMT exhibits 2D lamellar morphology with 10–20 μm in width and 0.5–2 μm in thickness. The SEM image of RGO-MMT (Fig. 2c) indicates MMT and RGO nanosheets are stacked with each other, which exhibits layered structures. In the TEM image of RGO-MMT (Fig. 2d), RGO nanosheets cover on the surface of MMT, which ensures the uniform distribution of MMT and RGO. In the SA/MMT (Fig. 2e), MMT was wrapped with the

continuous SA to form a block. From the SEM image of SA/RGO-MMT (Fig. 2f), the layered structures of RGO-MMT could be observed, and SA is filled in the layered structures, which contributes to the interfacial thermal transfer between SA and the supporting materials.

The phase structures of samples were investigated by X-ray diffraction (XRD), and the XRD patterns are shown in Fig. 3. The reflection at 1.2 nm is found in the XRD pattern of MMT, which is corresponding to (001) basal spacing of Na-montmorillonite[33]. The XRD pattern of SA exhibits two obvious reflections of stearic acid at 21.5° and 23.8°. The XRD pattern of RGO-MMT is similar with that of MMT, and no obvious reflection is attributed to the RGO. The reflections corresponding to MMT and SA could be found in the XRD patterns of SA/MMT and SA/RGO-MMT, and the phase of SA possesses high crystallinity. The reflection intensity of MMT in SA/RGO-MMT is relatively lower than that of SA/MMT, which suggests the higher content of SA and thermal storage capacity in SA/RGO-MMT.

The vibrational bands and interfacial characteristics of samples were studied by Fourier transform infrared (FTIR) spectra[34] (Fig. 4). In the FTIR spectrum of MMT, the bands at 1022 and 471 cm^{-1} are corresponding to the stretching and bending vibration of Si-O in silicon-oxygen tetrahedron. The bands at 3620 and 1637 cm^{-1} are assigned to the stretching and bending vibration of hydroxyl groups, and the broad bands at 3453 cm^{-1} are ascribed to stretching vibrations of H-O-H in water [35, 36]. For SA, the bands corresponding to $-\text{CH}_2$ and $-\text{CH}_3$ are found at 2918, 2849, 1466 and 723 cm^{-1} , and the band at 1703 cm^{-1} is attributed to the vibration of C = O. Compared with FTIR spectrum of MMT, that of RGO-MMT exhibits less hydroxyl groups, which might be because the hydroxyl groups on the surface of MMT are covered or removed due to the modification of RGO. The bands ascribed to MMT and SA are found in the FTIR spectra of SA/MMT and SA/RGO-MMT, and no obvious shift of band was observed, indicating the physical interactions between SA and RGO-MMT. The band intensity of SA in SA/RGO-MMT is relatively higher than that in SA/MMT, which might be due to the higher content of SA in according with the result of XRD.

The energy storage capacity is one of the most critical parameters for phase change material. The phase change properties of SA, SA/MMT and SA/RGO-MMT are analyzed via the differential scanning calorimetry (DSC) method (Fig. 5), and the corresponding phase change temperature and enthalpy are listed in Table 1. The pristine SA has a melting enthalpy of 208 J/g with the melting temperature of 54.9 °C and a freezing enthalpy of 212 J/g with the freezing temperature of 53.0 °C, respectively. The melting and freezing enthalpies of SA/RGO-MMT are 159 and 165 J/g, which are rather higher than that of SA/MMT (59 and 52 J/g). It is because that SA/RGO-MMT has higher content of SA, which has been confirmed by XRD and FTIR analysis.

Table 1

Thermal properties of SA, SA/MMT, SA/RGO-MMT before and after thermal cycling.

Samples	Melting temperature ($T_m, ^\circ\text{C}$)	Freezing temperature ($T_f, ^\circ\text{C}$)	Melting enthalpy ($\Delta H_m, \text{J/g}$)	Freezing enthalpy ($\Delta H_f, \text{J/g}$)	Extent of supercooling ($T_m - T_f, ^\circ\text{C}$)
SA	54.9	53.0	208	212	1.9
SA/MMT	53.5	50.4	59	52	3.1
SA/MMT-RGO	52.8	51.4	159	165	1.4
SA/MMT-RGO after thermal cycling	52.9	51.6	155	163	1.3

Compared with the reported composite PCMs in the literatures (Table 2) [25, 37–40], SA/RGO-MMT possesses highly competitive energy storage capacity. The extent of supercooling of SA/RGO-MMT is 1.4 $^\circ\text{C}$, lower than that of pristine SA (1.9 $^\circ\text{C}$) and SA/ MMT (3.1 $^\circ\text{C}$). The lower extent of supercooling of SA/RGO-MMT is beneficial in energy storage process of phase change, which could be attributed to the higher heat transfer efficiency in SA/RGO-MMT.

Table 2

Comparison of thermal properties of SA/MMT-RGO with the reported composite PCMs.

Composite PCMs	Melting temperature ($T_m, ^\circ\text{C}$)	Freezing temperature ($T_f, ^\circ\text{C}$)	Melting enthalpy ($\Delta H_m, \text{J/g}$)	Freezing enthalpy ($\Delta H_f, \text{J/g}$)	References
Stearic acid/mesoporous SiO_2 microspheres	71.5	62.4	135.3	133.5	[37]
Stearic acid/halloysite	53.7	49.1	106	107	[38]
Stearic acid/activated montmorillonite	59.9	55.1	85	89	[25]
Stearic acid/graphene microcapsule	72.0	64.0	166	163	[39]
Stearic acid/graphite and activated bentonite	53.4	52.9	85	84	[40]
SA/MMT-RGO	52.8	51.4	159	165	This work

Energy storage and release rates of phase change material have great influence in practical application of energy storage. Thermal storage and release performances of SA, SA/MMT and SA/RGO-MMT were evaluated via temperature variation curve over time (Fig. 6). The time period of SA/RGO-MMT from the ambient temperature to melting temperature is 163 s, much less than that of SA (410 s) and SA/MMT (360 s). Compared with SA, MMT and RGO-MMT in SA/MMT and SA/RGO-MMT could enhance heat transfer of composite phase change materials. Furthermore, SA/RGO-MMT possesses faster heating rate than SA/MMT due to the higher interfacial thermal transfer efficiency. As shown in Fig. 7a, the thermal conductivity of MMT-RGO is $0.921 \text{ Wm}^{-1}\text{K}^{-1}$, which is more than twice that of MMT ($0.372 \text{ Wm}^{-1}\text{K}^{-1}$). The graphene with high thermal conductivity connects between SA and MMT, which could greatly enhance the interfacial thermal transfer in SA/RGO-MMT (Fig. 7b). SA/RGO-MMT has fastest cooling rate from $80 \text{ }^{\circ}\text{C}$ to the ambient temperature, the cooling process of which only takes about 1070s. SA/RGO-MMT possesses faster heating and cooling rates, indicating the higher energy storage and release efficiency and less time cost during energy storage utilization.

Figure 7. (a) Thermal conductivity of MMT-RGO and MMT, (b) interfacial structure and thermal transfer of SA/RGO-MMT

Thermal reliability plays a significant role in the energy storage application of phase change material. The properties of SA/RGO-MMT before and after 100 thermal cycling are compared to evaluate the thermal storage and release stability. The XRD patterns and FTIR spectra of SA/RGO-MMT before and after thermal cycling (Fig. 8a and b) exhibit no remarkable difference, indicating the thermal cycling makes little impact on phase structures and interfacial characteristics of SA/RGO-MMT. From the SEM images of SA/RGO-MMT before and after thermal cycling (Fig. 8c and d), the morphology of SA/RGO-MMT appears little change with only a few agglomerations, which is favor for heat transfer. The melting and freezing enthalpies of SA/RGO-MMT have a negligible reduction after thermal cycling (Fig. 8e), and the extent of supercooling decreases slightly. The thermal storage and release curves of SA/RGO-MMT before and after thermal cycling (Fig. 8f) are similar, and the energy storage and release rates remain unchanged. Therefore, SA/RGO-MMT has excellent thermal reliability after 100 thermal cycling.

Figure 8. (a) XRD patterns, (b) FTIR spectra, SEM images of (c) before and (d) after thermal cycling, (e) DSC curves and (f) thermal storage and release curves of SA/RGO-MMT before and after 100 thermal cycling.

Conclusions

In summary, RGO-MMT was obtained via the in situ reduction of GO on the surface of MMT, and SA/RGO-MMT was prepared by the vacuum impregnation of SA into RGO-MMT matrix. The SA content of SA/RGO-MMT is higher than that of SA-MMT, and SA is filled in the layered structures of RGO-MMT with the physical interactions. SA/RGO-MMT possesses high melting and freezing enthalpies of 159 and 165 J/g and low extent of supercooling of $1.4 \text{ }^{\circ}\text{C}$. Energy storage and release rates of SA/RGO-MMT were improved due to the enhanced interfacial thermal transfer by graphene. SA/RGO-MMT has excellent

thermal reliability after 100 thermal cycling. The excellent performance of SA/RGO-MMT makes it promising application in solar heat storage. The strategy of interface modification with graphene paves a new avenue to enhance thermal transfer for the efficient thermal energy storage materials.

Declarations

Acknowledgments

This work was supported by National Natural Science Foundation of China (51804242, 51772237, 51704030), the China Postdoctoral Science Foundation (2018T111054, 2019T120870, 2017M623182, 2017M610617), China Scholarship Council (201906285057), Natural Science Basic Research Plan in Shaanxi province of China (2019JQ-693), the Young Talent fund of University Association for Science and Technology in Shaanxi (20180411), Shaanxi Postdoctoral Science Foundation (2017BSHEDZZ10), the Fundamental Research Funds for the Central Universities (300102319203). We thank Dr. Jiamei Liu, Zijun Ren and Chao Li at Instrument Analysis Center of Xi'an Jiaotong University for XPS, SEM and TEM measurements.

Authors' Contributions

KP and HW developed the concept. KP and XL designed the experiments, synthesized and characterized the materials. KP wrote the final paper. KP, HW and XL wrote the initial drafts. All authors analysed the data, discussed the results and commented on the manuscript. All authors read and approved the final manuscript.

Competing Interests

The authors declare that they have no competing interests.

References

1. Min P, Liu J, Li X, An F, Liu P, Shen Y, Koratkar N, Yu Z-Z (2018) Thermally conductive phase change composites featuring anisotropic graphene aerogels for real-time and fast-charging solar-thermal energy conversion. *Adv Funct Mater* 28:1805365.
2. Han G G D, Li H, Grossman J C (2017) Optically-controlled long-term storage and release of thermal energy in phase-change materials. *Nat Comm* 8:1446.
3. Li G, Hong G, Dong D, Song W, Zhang X (2018) Multiresponsive graphene-aerogel-directed phase-change smart fibers. *Adv Mater* 30:1801754.

4. Zhang W, Ji X, Peng B-J, Che S, Ge F, Liu W, Al-Hashimi M, Wang C, Fang L (2019) High-Performance Thermoresponsive Dual-Output Dye System for Smart Textile Application. *Adv Funct Mater*:1906463.
5. Shi Y, Wang C, Yin Y, Li Y, Xing Y, Song J (2019) Functional Soft Composites As Thermal Protecting Substrates for Wearable Electronics. *Adv Funct Mater* 29:1905470.
6. Peng K, Fu L, Li X, Ouyang J, Yang H (2017) Stearic acid modified montmorillonite as emerging microcapsules for thermal energy storage. *Appl Clay Sci* 138:100-106.
7. Tao P, Chang C, Tong Z, Bao H, Song C, Wu J, Shang W, Deng T (2019) Magnetically-accelerated large-capacity solar-thermal energy storage within high-temperature phase-change materials. *Energy Environ Sci* 12:1613-1621.
8. Peng K, Zhang J, Yang H, Ouyang J (2015) Acid-hybridized expanded perlite as a composite phase-change material in wallboards. *RSC Adv* 5:66134-66140.
9. Gao H, Wang J, Chen X, Wang G, Huang X, Li A, Dong W (2018) Nanoconfinement effects on thermal properties of nanoporous shape-stabilized composite PCMs: A review. *Nano Energy* 53:769-797.
10. Chen X, Gao H, Yang M, Dong W, Huang X, Li A, Dong C, Wang G (2018) Highly graphitized 3D network carbon for shape-stabilized composite PCMs with superior thermal energy harvesting. *Nano Energy* 49:86-94.
11. Liu Z, Zou R, Lin Z, Gui X, Chen R, Lin J, Shang Y, Cao A (2013) Tailoring carbon nanotube density for modulating electro-to-heat conversion in phase change composites. *Nano Lett* 13:4028-4035.
12. Wang J, Yang M, Lu Y, Jin Z, Tan L, Gao H, Fan S, Dong W, Wang G (2016) Surface functionalization engineering driven crystallization behavior of polyethylene glycol confined in mesoporous silica for shape-stabilized phase change materials. *Nano Energy* 19:78-87.
13. Li X, Peng K (2018) Synthesis of 3D mesoporous alumina from natural clays for confining CdS nanoparticles and enhanced photocatalytic performances. *Appl Clay Sci* 165:188-196.
14. Aftab W, Huang X, Wu W, Liang Z, Mahmood A, Zou R (2018) Nanoconfined phase change materials for thermal energy applications. *Energy Environ Sci* 11:1392-1424.
15. Peng K, Fu L, Yang H, Ouyang J, Tang A (2017) Hierarchical MoS₂ intercalated clay hybrid nanosheets with enhanced catalytic activity. *Nano Res* 10:570-583.
16. Peng K, Fu L, Ouyang J, Yang H (2016) Emerging parallel dual 2D composites: Natural clay mineral hybridizing MoS₂ and interfacial structure. *Adv Funct Mater* 26:2666-2675.
17. Peng K, Wang H, Li X, Wang J, Xu L, Gao H, Niu M, Ma M, Yang J (2019) One-step hydrothermal growth of MoS₂ nanosheets/CdS nanoparticles heterostructures on montmorillonite for enhanced visible light photocatalytic activity. *Appl Clay Sci* 175:86-93.
18. Yuan Y, Zhao S, Wen J, Wang D, Guo X, Xu L, Wang X, Wang N (2019) Rational Design of Porous Nanofiber Adsorbent by Blow-Spinning with Ultrahigh Uranium Recovery Capacity from Seawater. *Adv Funct Mater* 29:1805380.
19. Liu S, Yang H (2015) Composite of Coal-Series Kaolinite and Capric-Lauric Acid as Form-Stable Phase-Change Material. *Energy Technol* 3:77-83.

20. Cui Z-K, Kim S, Baljon J J, Wu B M, Aghaloo T, Lee M (2019) Microporous methacrylated glycol chitosan-montmorillonite nanocomposite hydrogel for bone tissue engineering. *Nat Comm* 10:3523.
21. Li X, Peng K, Dou Y, Chen J, Zhang Y, An G (2018) Facile synthesis of wormhole-like mesoporous tin oxide via evaporation-induced self-assembly and the enhanced gas-sensing properties. *Nanoscale Res Lett* 13:14.
22. Li X, Peng K (2018) Hydrothermal synthesis of MoS₂ nanosheet/palygorskite nanofiber hybrid nanostructures for enhanced catalytic activity. *Appl Clay Sci* 162:175-181.
23. Li X, Peng K (2018) MoSe₂/montmorillonite composite nanosheets: hydrothermal synthesis, structural characteristics, and enhanced photocatalytic activity. *Minerals* 8:268.
24. Li X, Peng K, Chen H, Wang Z (2018) TiO₂ nanoparticles assembled on kaolinites with different morphologies for efficient photocatalytic performance. *Sci Rep* 8:11663.
25. Wang Y, Zheng H, Feng H X, Zhang D Y (2012) Effect of preparation methods on the structure and thermal properties of stearic acid/activated montmorillonite phase change materials. *Ene Bui* 47:467-473.
26. Wang M, Zhang T, Mao D, Yao Y, Zeng X, Ren L, Cai Q, Mateti S, Li L H, Zeng X, Du G, Sun R, Chen Y, Xu J-B, Wong C-P (2019) Highly Compressive Boron Nitride Nanotube Aerogels Reinforced with Reduced Graphene Oxide. *ACS Nano* 13:7402-7409.
27. Jeong S-G, Jin Chang S, We S, Kim S (2015) Energy efficient thermal storage montmorillonite with phase change material containing exfoliated graphite nanoplatelets. *Solar Energy Mater Solar Cells* 139:65-70.
28. Gao X, Zhou J, Du R, Xie Z, Deng S, Liu R, Liu Z, Zhang J (2016) Robust Superhydrophobic Foam: A Graphdiyne-Based Hierarchical Architecture for Oil/Water Separation. *Adv Mater* 28:168-173.
29. Xu X, Zhang Q, Yu Y, Chen W, Hu H, Li H (2016) Naturally Dried Graphene Aerogels with Superelasticity and Tunable Poisson's Ratio. *Adv Mater* 28:9223-9230.
30. Zheng Z, Chang Z, Xu G-K, McBride F, Ho A, Zhuola Z, Michailidis M, Li W, Raval R, Akhtar R, Shchukin D (2016) Microencapsulated phase change materials in solar-thermal conversion systems: understanding geometry-dependent heating efficiency and system reliability. *ACS Nano* 11:721-729.
31. Zhou M, Lin T, Huang F, Zhong Y, Wang Z, Tang Y, Bi H, Wan D, Lin J (2013) Highly conductive porous graphene/ceramic composites for heat transfer and thermal energy storage. *Adv Funct Mater* 23:2263-2269.
32. WS H, RE O (1958) Preparation of graphite oxide. *J Am Chem Soc* 80:1339.
33. Peng K, Wang J, Wang H, Li X, Wan P, Zhang H, Bai L (2019) MoS₂ nanosheets supported on carbon hybridized montmorillonite as an efficient heterogeneous catalyst in aqueous phase. *Appl Clay Sci* 183:105346.
34. Liu W, Xu J, Han J, Jiao F, Qin W, Li Z (2018) Kinetic and mechanism studies on pyrolysis of printed circuit boards in the absence and presence of copper. *ACS Sustainable Chem. & Eng.* 7:1879-1889.

35. Peng K, Wang H, Li X, Wang J, Cai Z, Su L, Fan X (2019) Emerging WS₂/montmorillonite composite nanosheets as an efficient hydrophilic photocatalyst for aqueous phase reactions. *Sci Rep* 9:16325.
36. Chen W, Hu Y, Lv W, Lei T, Wang X, Li Z, Zhang M, Huang J, Du X, Yan Y, He W, Liu C, Liao M, Zhang W, Xiong J, Yan C (2019) Lithiophilic montmorillonite serves as lithium ion reservoir to facilitate uniform lithium deposition. *Nat Comm* 10:4973.
37. Fan S, Gao H, Dong W, Tang J, Wang J, Yang M, Wang G (2017) Shape-stabilized phase change materials based on stearic acid and mesoporous Hollow SiO₂ microspheres (SA/SiO₂) for thermal energy storage. *Eur J Inorg Chem* 2017:2138-2143.
38. Mei D, Zhang B, Liu R, Zhang H, Liu J (2011) Preparation of stearic acid/halloysite nanotube composite as form-stable PCM for thermal energy storage. *Int J Energ Res* 35:828-834.
39. Dao T D, Jeong H M (2015) Novel stearic acid/graphene core-shell composite microcapsule as a phase change material exhibiting high shape stability and performance. *Solar Energy Mater Solar Cells* 137:227-234.
40. Li C, Fu L, Ouyang J, Yang H (2013) Enhanced performance and interfacial investigation of mineral-based composite phase change materials for thermal energy storage. *Sci Rep* 3:1-8.

Figures

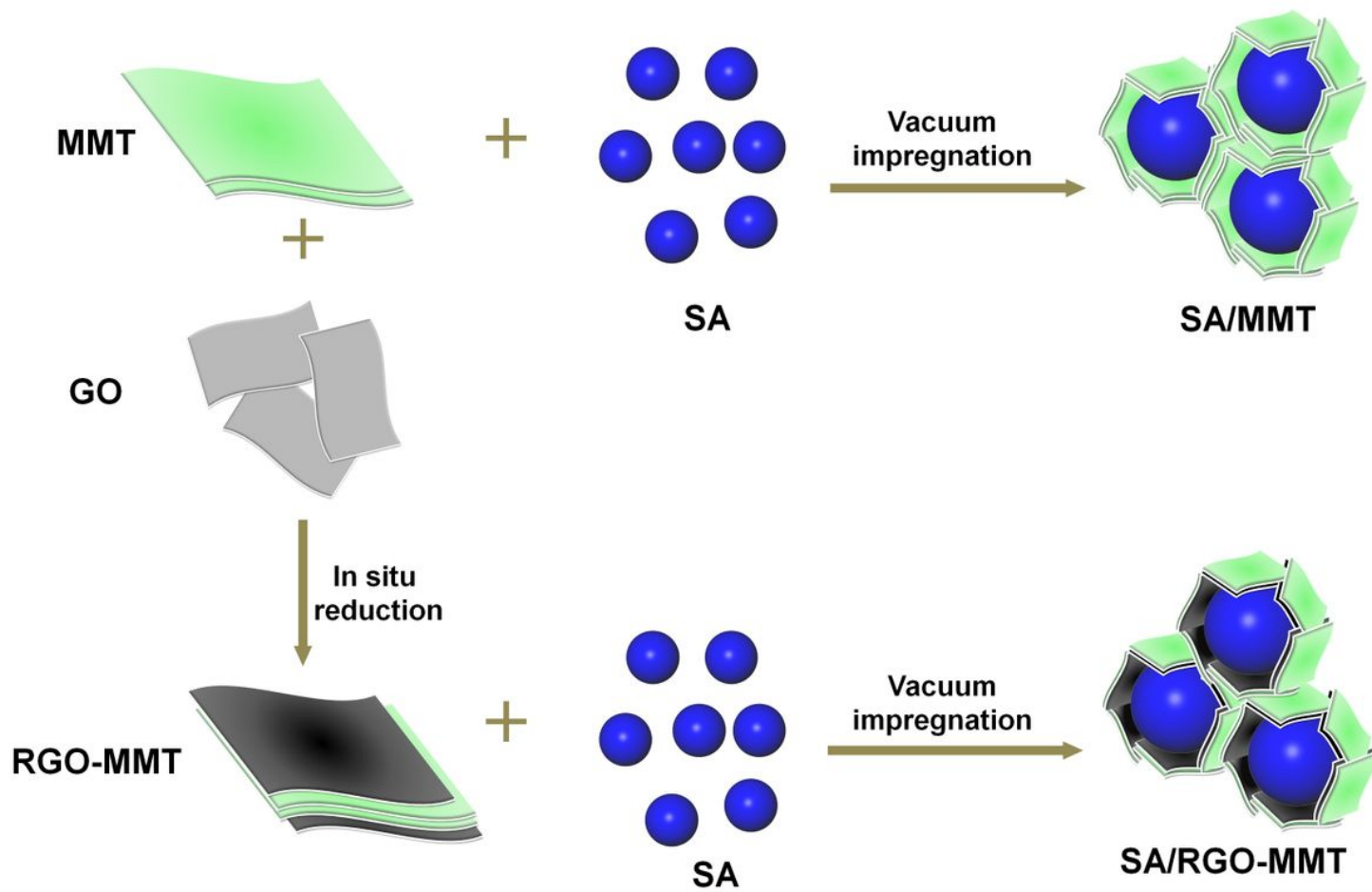


Figure 1

Schematically synthetic process of SA/MMT and SA/RGO-MMT.

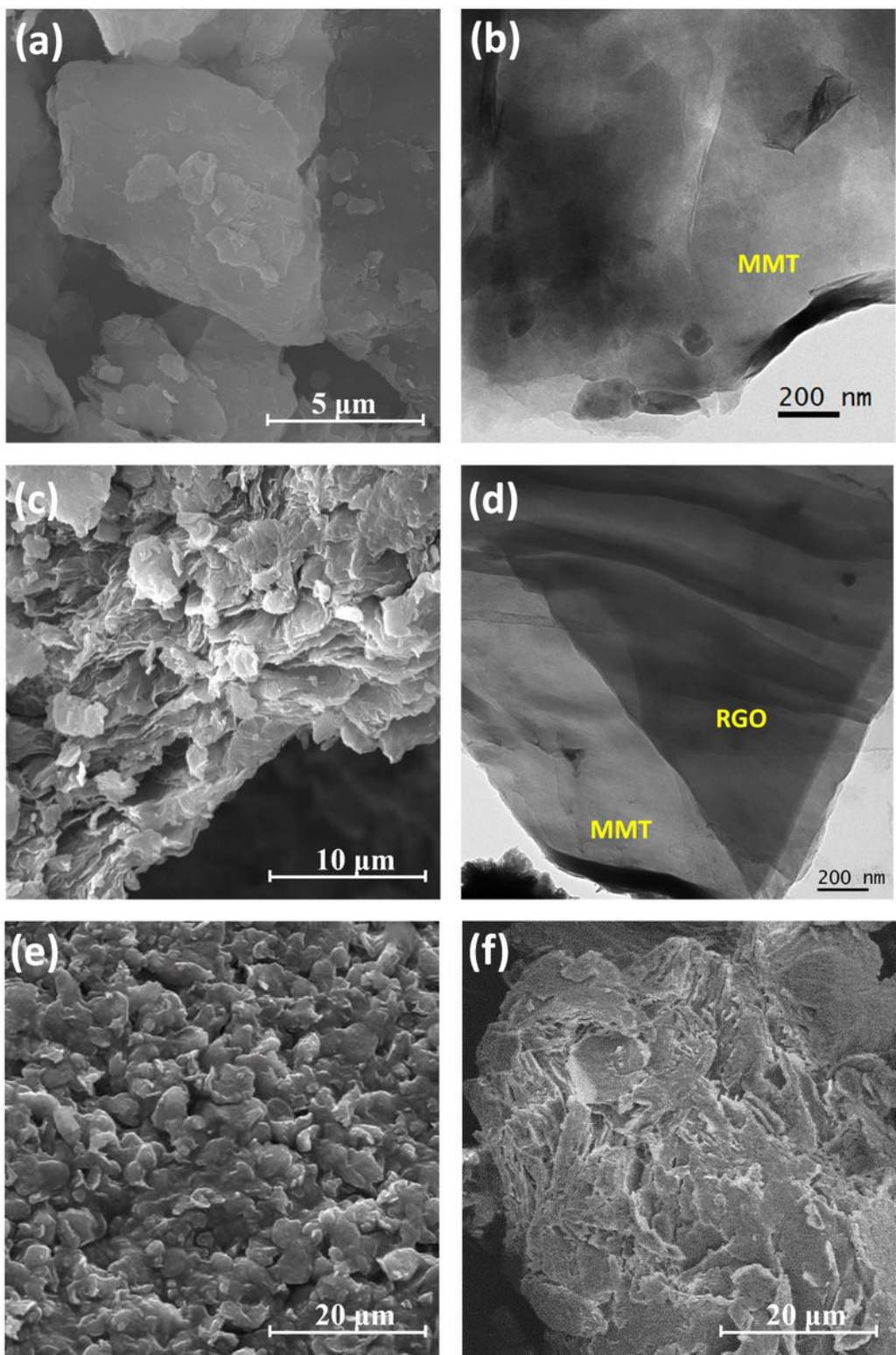


Figure 2

SEM images of (a) MMT, (c) RGO-MMT, (e) SA/MMT and (f) SA/RGO-MMT, TEM images of (b) MMT, d) RGO-MMT.

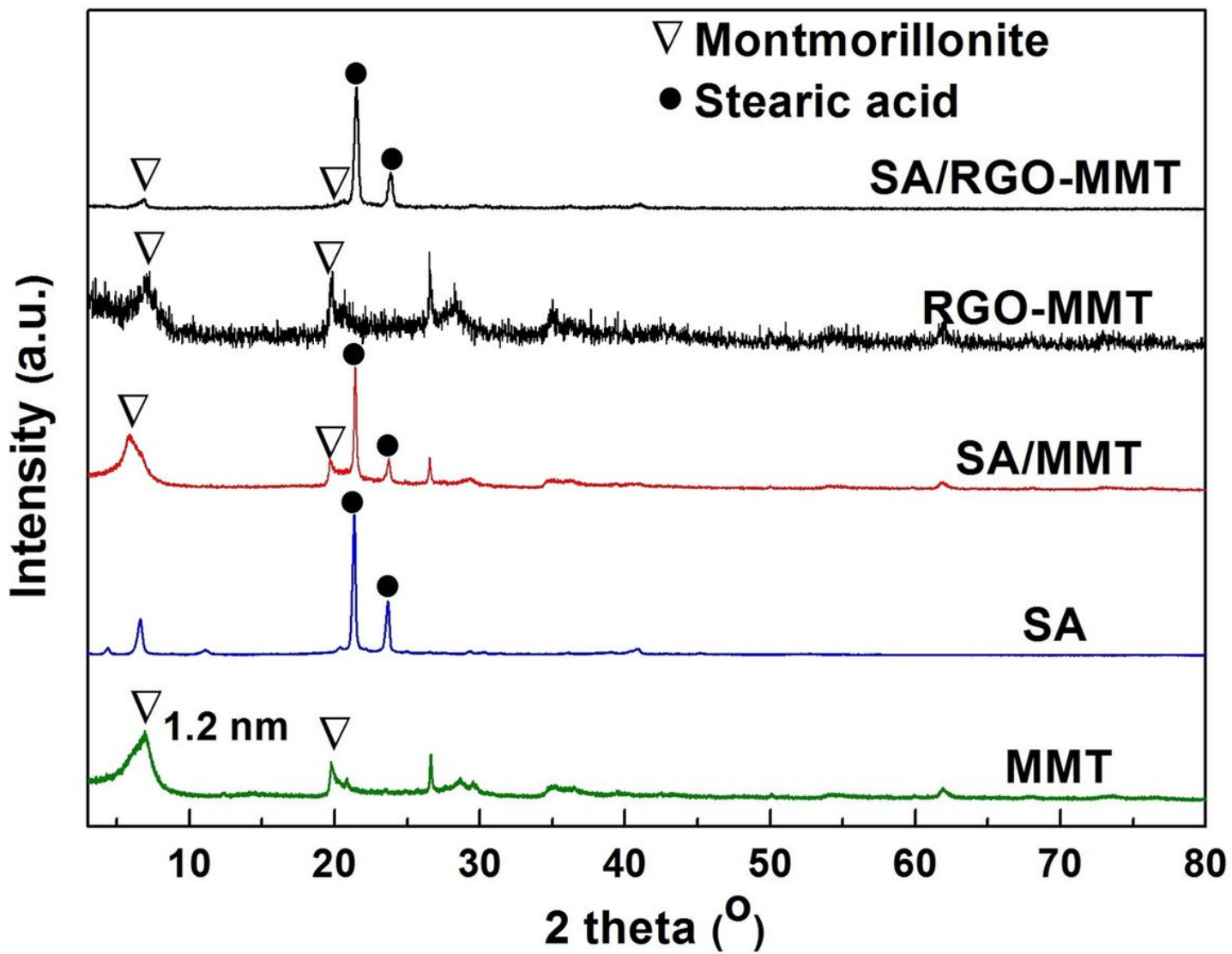


Figure 3

XRD patterns of SA, MMT, SA/MMT, RGO-MMT and SA/RGO-MMT.

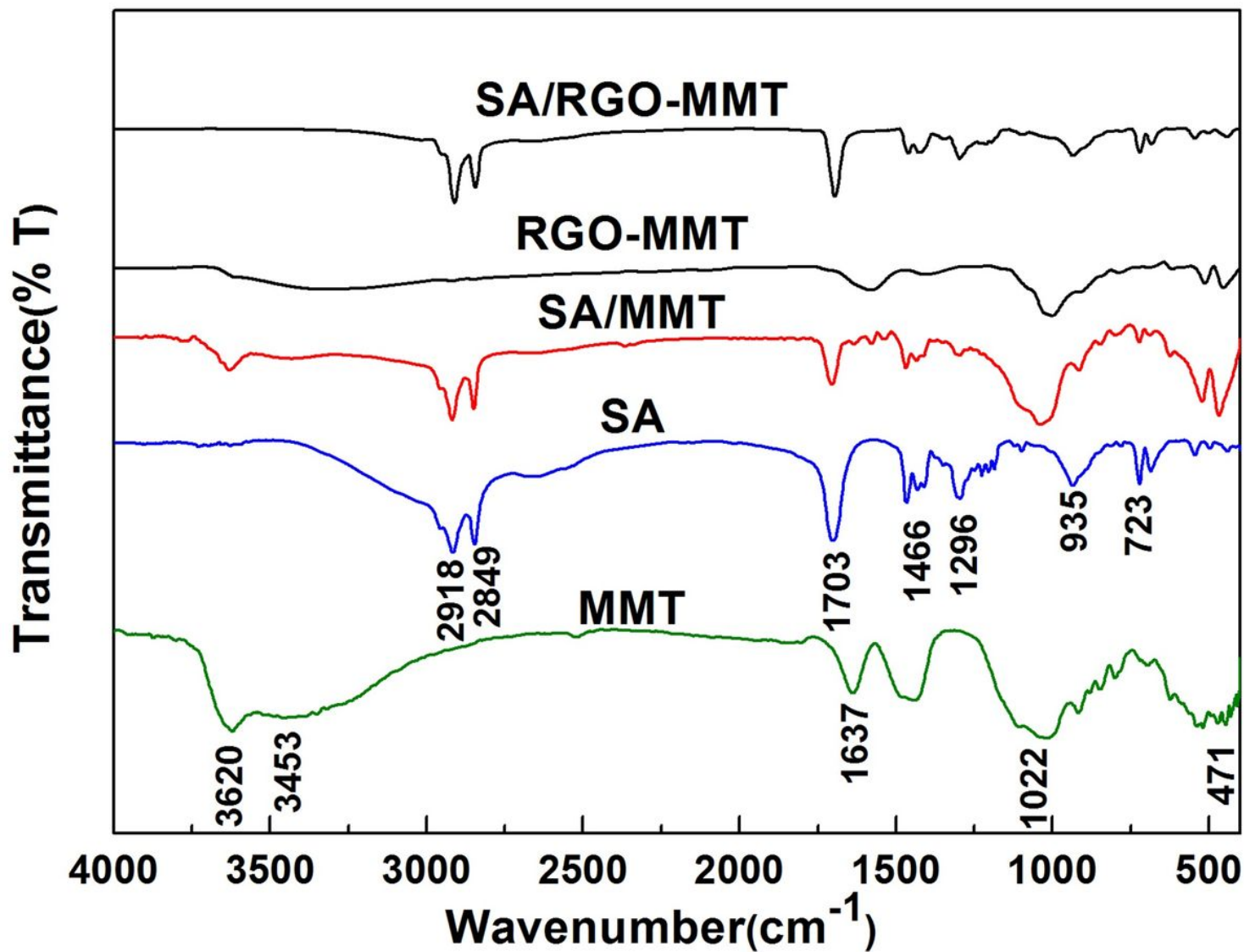


Figure 4

FTIR spectra of SA, MMT, SA/MMT, RGO-MMT and SA/RGO-MMT.

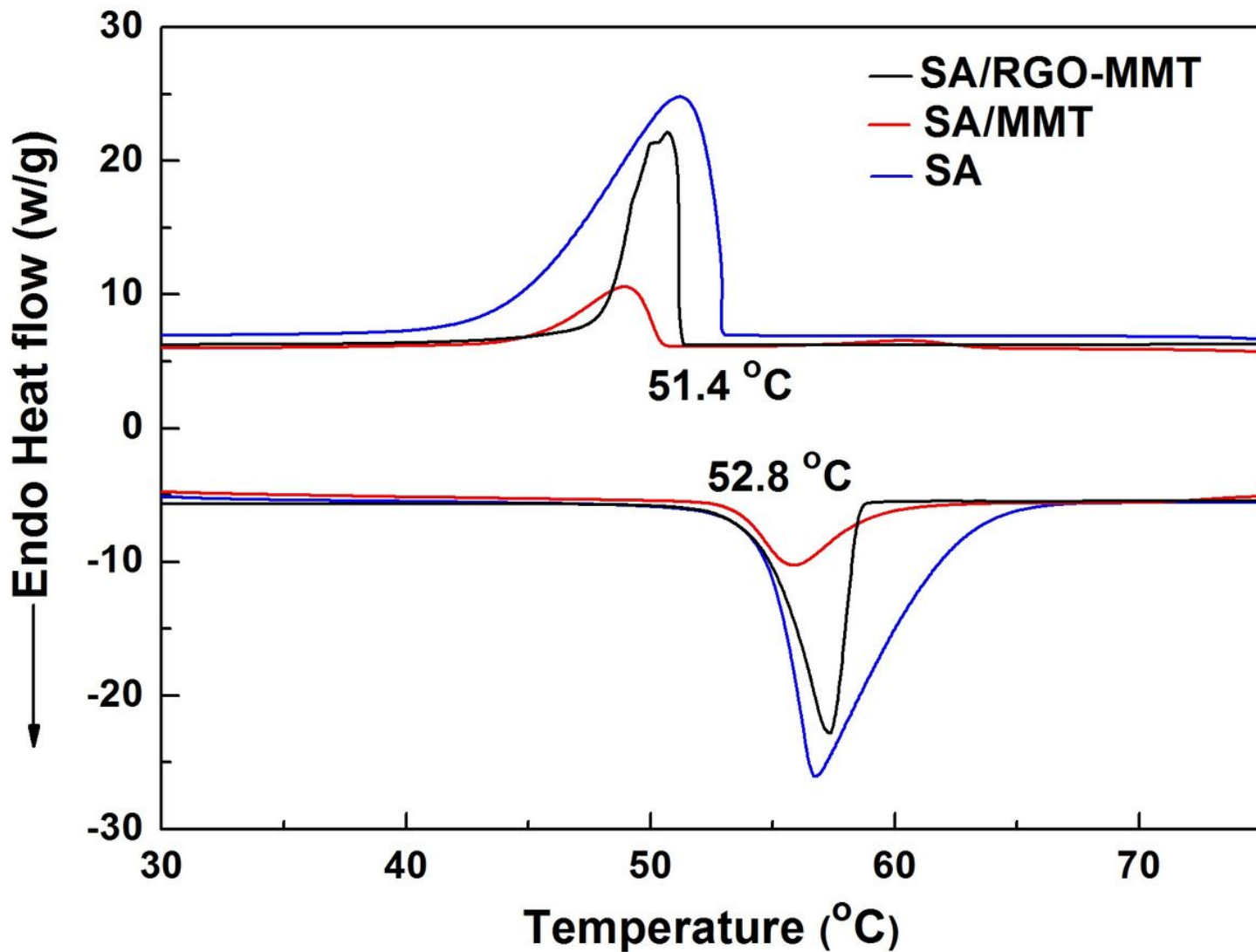


Figure 5

DSC curves of SA, SA/MMT, SA/RGO-MMT.

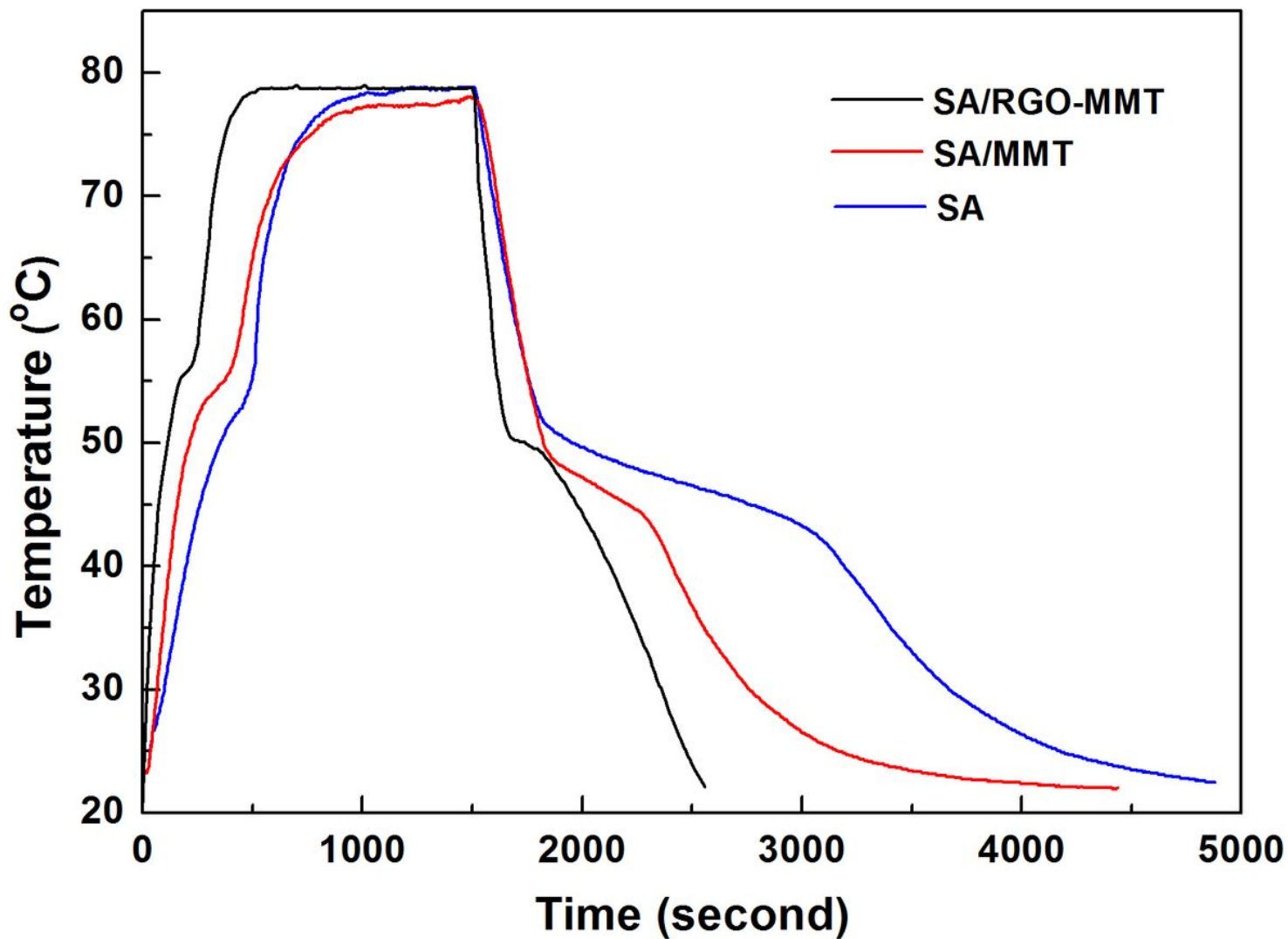


Figure 6

Thermal storage and release curves of SA, SA/MMT, SA/RGO-MMT.

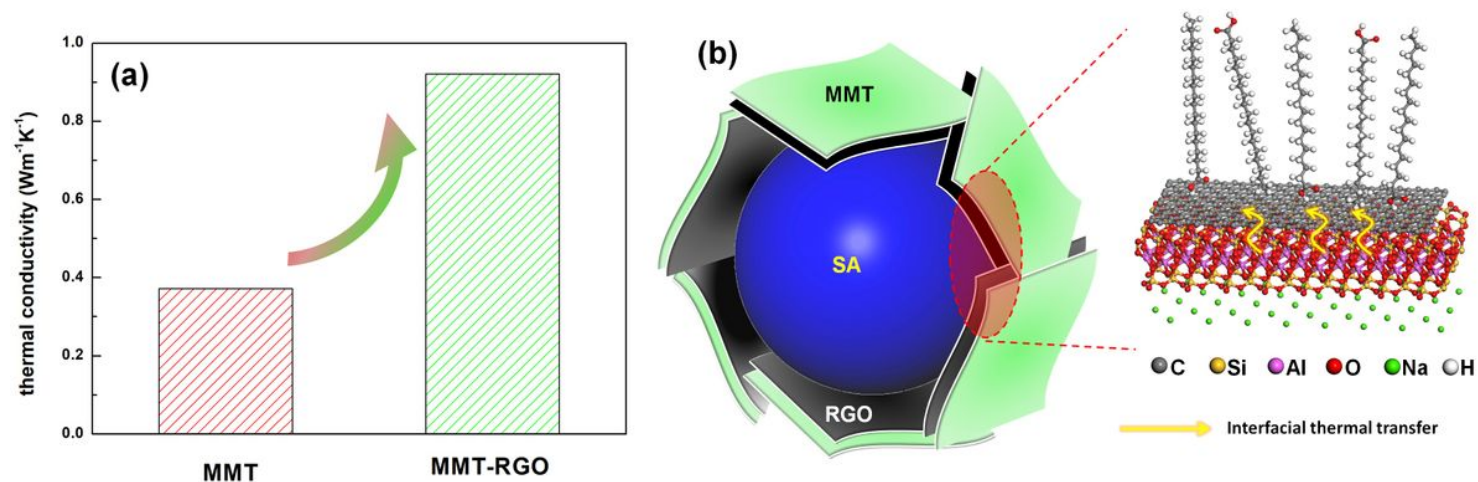


Figure 7

(a) Thermal conductivity of MMT-RGO and MMT, (b) interfacial structure and thermal transfer of SA/RGO-MMT

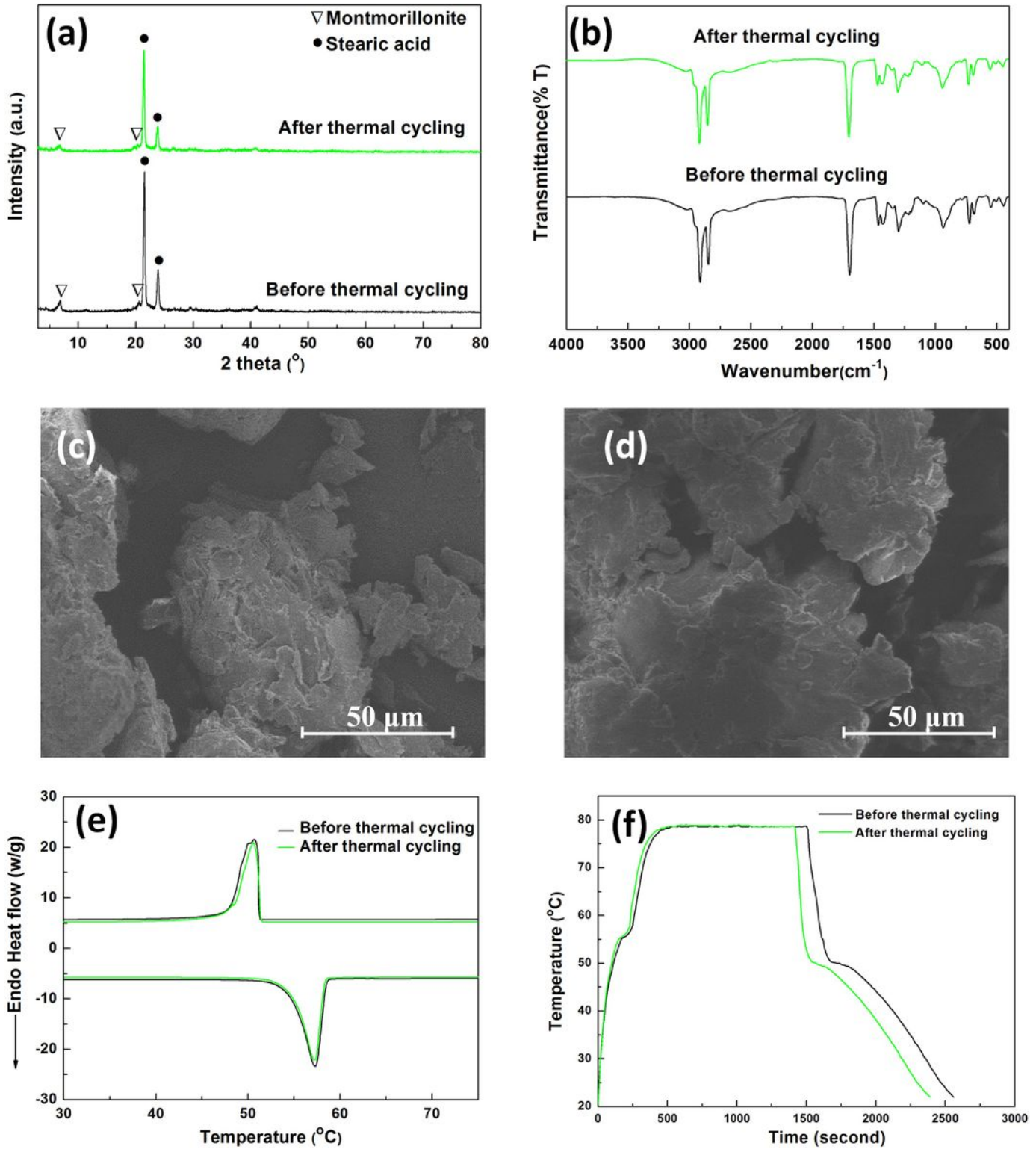


Figure 8

(a) XRD patterns, (b) FTIR spectra, SEM images of (c) before and (d) after thermal cycling, (e) DSC curves and (f) thermal storage and release curves of SA/RGO-MMT before and after 100 thermal cycling.